



Production of magnetic biochar from waste-derived fungal biomass for phosphorus removal and recovery

Joshua Jack^{a, b}, Tyler M. Huggins^a, Yingping Huang^c, Yanfen Fang^{c, **},
Zhiyong Jason Ren^{a, d, *}

^a Department of Civil, Environmental and Architectural Engineering, University of Colorado Boulder, Boulder, CO, USA

^b Biosciences Center, National Renewable Energy Laboratory, Golden, CO, USA

^c Hubei Province Collaborative Innovation Center for Geological Hazards and Ecology in the Three Gorges Region, Yichang, Hubei, China

^d Department of Civil and Environmental Engineering and The Andlinger Center for Energy and the Environment, Princeton University, Princeton, NJ, USA

ARTICLE INFO

Article history:

Received 6 November 2018

Received in revised form

7 February 2019

Accepted 11 March 2019

Available online 14 March 2019

Keywords:

Magnetic biochar

Iron impregnation

Neurospora crassa

Wastewater

Phosphorus

Biofabrication

ABSTRACT

This study presents a new bottom-up biofabrication method to produce highly porous magnetic biochar from waste-derived fungal biomass. *Neurospora crassa* was grown in iron containing coagulation backwash (BW) diluted with primary effluent (PE) wastewater in two ratios of 1:4 (PE-BW 1:4) and 3:4 (PE-BW 3:4). The fungi encapsulated iron directly into biomass hyphae and carbonization resulted in one-step biochar preparation and maghemite (Fe_2O_3) formation. The morphology and structure of the materials were investigated using a suite of characterization tools. Results indicated that the physiochemical properties of each char were dependent on the blend used for fungal cultivation. PE-BW 1:4 had much larger average pore diameters (13.2 nm vs. 6.1 nm), less elemental surface carbon (2.1% vs. 23.7%), and more expansive Fe_2O_3 formation. Batch phosphorus adsorption experiments were conducted in the range of 0–90 mg-P/L, and a maximum adsorption density of 23.9 mg/g was achieved. Langmuir, Freundlich and Temkin isotherms were used to describe the interactions of the phosphate on the adsorbents and an in-depth error analysis was conducted. Further characterization of the P-loaded chars indicated adsorption primarily via P-OH bonding on the surface of the materials. This new biofabrication method showed great potential to magnetic biochar production with excellent phosphorus adsorption, which can be effectively used in wastewater resource recovery.

© 2019 Elsevier Ltd. All rights reserved.

1. Introduction

Phosphorus is an essential element for life, but excess amounts of phosphorus released from agricultural runoff or municipal wastewater can have negative impacts in aquatic ecosystems (Jung et al., 2017). As such, development of efficient and sustainable methods that remove phosphorus from wastewater and recover it as fertilizer hold great potential. Various methods involving biological treatment, membrane separation, chemical precipitation, electrolysis and adsorption have been investigated (Huggins et al., 2016; Pan et al., 2017). Of these technologies, phosphorus

adsorption onto biochar is considered to be a promising method due to its low cost, high selectivity, eco-friendliness, and ease of operation (Jiang et al., 2017; Li et al., 2016).

A recent study demonstrated maximum phosphate adsorption capacities of 0.036 mg/g, 0.132 mg/g, and 0.296 mg/g using corn-cob, garden wood waste, and wood chips biochars, respectively (Michalekova-Richveisova et al., 2017). Others, however, have demonstrated far better phosphorus adsorption capabilities using biochars modified with iron particles. For example, Cai et al. (2017) reported a maximum phosphate adsorption of 5.07 mg/g using magnetic biochar derived from water hyacinth. Notably, the modification of biochars with iron does not only make biochar a better adsorbent for some contaminants but also holds the added benefits of easy removal and recovery using simple magnets (Ruining Li et al., 2018).

Though beneficial, the production of most magnetic biochars can be quite complicated and unsustainable. The majority of current methods involve a set of secondary processes in which a

* Corresponding author. Department of Civil, Environmental and Architectural Engineering, University of Colorado Boulder, Boulder, CO, USA.

** Corresponding author.

E-mail addresses: chem_ctgu@126.com (Y. Fang), Zhiyong.Ren@colorado.edu (Z.J. Ren).

magnetic medium is deposited on the surface of a char (Chen et al., 2011; Reza et al., 2015). For instance, Wang et al. (2015) prepared magnetic pine wood biochar by mineralizing hematite and mixing the suspension with the feedstock material prior to pyrolysis. Alternatively, Yang et al. (2018) impregnated iron directly into waste-activated sludge biomass prior to pyrolysis and found the phosphorus adsorption capabilities were greatly improved compared to samples fabricated using deposition methods. Nevertheless, current methods involve the use of expensive chemicals, complicated processing techniques, and generation of complex wastes.

In this work, we present a simple and novel bottom-up method for magnetic biochar production that alleviates these drawbacks and demonstrates excellent performance. Unique to our method, iron precursors are not impregnated in the char nor deposited onto the biochar post-pyrolysis, but rather accumulated and encapsulated within the living biomass feedstock prior to processing. The key to this innovative approach is the use of widely available municipal waste streams in combination with the robust fungus, *Neurospora crassa* (*N. crassa*), to generate biomass as the feedstock material for pyrolysis. *N. crassa* is capable of bio-accumulating high concentrations of many metals such as iron, cobalt, and nickel at high yields without affecting biomass growth (Babu et al., 2018; Castro et al., 2011; Mukherjee et al., 2008). Furthermore, *N. crassa* is easy to culture and exhibits a rapid growth rate on many minimal media. As such, *N. crassa* has been used in a wide variety of biological studies and its genome has been thoroughly mapped making it amenable to genetic manipulation (Borkovich et al., 2004). The culmination of these unique qualities allow for a cheap, sustainable and adaptable source of biomass.

N. crassa is grown directly in iron-rich wastewater streams, which not only enables magnetic biochar production but also accomplishes wastewater treatment by removing metals and organics from the waste stream. Typical waste streams can be from water treatment plants that use iron coagulants and primary effluent from wastewater treatment or industrial wastewater streams.

Here we demonstrated for the first time that *N. crassa* wild type could be grown on blends of waste streams, and the resulting biomass could be effectively processed into a magnetic biochar material. We further demonstrate that the physiochemical properties of the materials could be tuned by controlling the relative volumes of each of the waste streams used in the growth media. This technique allows for a low-cost, versatile, and sustainable approach to create magnetic biochar directly from municipal waste. The structure and morphology of the processed chars were investigated using a suite of tools including scanning electron microscopy equipped with an energy-dispersive X-ray analyzer (SEM-EDS), BET-N₂ adsorption, X-ray photoelectron spectroscopy (XPS), X-ray powdered diffraction (XRD) and Fourier transform spectroscopy (FTIR). To confirm the adsorbent properties of these materials, batch phosphate adsorption studies were also conducted. Adsorption mechanisms were analyzed by fitting experimental data to Langmuir, Freundlich and Temkin isotherms and characterizing the P-loaded chars.

2. Materials and methods

2.1. Material production and processing

N. crassa was grown in waste streams consisting of primary effluent (PE) from Boulder wastewater treatment facility (Boulder, CO) and iron coagulation backwash (BW) from Boulder reservoir water treatment plant (Boulder, CO). Due to low organic content, BW alone was not able to sustain biomass growth so it was diluted

with PE at ratios of 1:4 (PE-BW 1:4) or 3:4 (PE-BW 3:4). Prior to use, both waste streams were autoclaved at 121 °C for 15 min. Glucose was then blended with waste streams at 1% (w/v) to stimulate the fungal acclimation. The major constituents of each growth blend prior to fungal inoculation were determined by inductively coupled plasma mass spectrometry (Perkin Elmer SCIEX-ICP-MS; Fig. S1).

N. crassa wild-type strain (FGSC #262) stock was stored on Vogel's minimal media slants (Vogel, 1964) at −20 °C. New cultures were initiated by growing cells on agar slants at 30 °C for 3 days in complete darkness. Conidia (fungal spores) were isolated from slants using standard methods and inoculated into 1 L flasks of media at a 1:100 dilution (Cockrell et al., 2015). After inoculation, fungal cultures were stored on an orbital incubator/shaker (Barnstead Max Q4000) at 30 °C and 90 rpm for 48 h. The resulting biomass was then harvested using a vacuum pump and 0.45 µm filters and dried in a desiccator for 24 h at 50 °C. The dry biomass was carbonized by heating the biomass to 700 °C at a rate of 10 °C/min of using an isotemp muffle furnace (Fischer Scientific-550 series) (Lu, et al., 2015). The resulting granular fungal char was then processed into a powder using a ball mill for 20 min (Retsch-PM100). It is expected that the particle size after grinding is less than 325 meshes. Fig. 1 summarizes the fabrication method of the magnetic biochar.

2.2. Material characterization

The magnetic properties of the chars were determined using a simple magnet. To test the stability of the magnetic properties, both chars were put into aqueous solution (pure water; 0.1 g/L) and rotated at 120 rpm for 14 days at 25 °C in the dark. The morphology and structure of the powdered biochars were investigated using SEM (Jeol JSM- 6480LV, 90 kV) (Lu et al., 2016a, b). The elemental composition of the materials were examined using EDS (Oxford Instruments Link ISIS) coupled to the SEM. Surface composition was further investigated using FTIR spectra recorded in the 4000–400 cm^{−1} region with a resolution of 4 cm (Bruker Vector 22 FTIR spectrometer) (Huggins et al., 2015). Further analysis of the

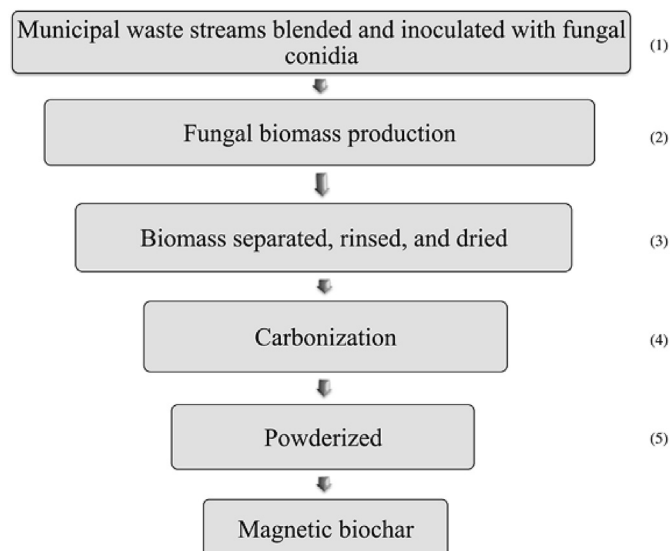


Fig. 1. Flow diagram for magnetic biochar production- Fungal biomass derived from waste streams processed into powdered magnetic biochar material. 1) Growth media prepared by blending waste-streams and inoculating fungal spores. 2) Fungal cultures grown for 48 h at 37 °C, agitated at 90 rpm. 3) Biomass filtered using 0.45 µm filter then dried in a desiccator at 50 °C for 24 h. 4) Dry biomass carbonized in a muffle furnace at 700 °C. 5) Granular material processed to a powder using a ball mill.

materials surfaces were conducted using X-ray photoelectron spectroscopy (PE-5800 X-ray Photoelectron Spectroscopy) performed in the range of 0–1100 eV. The surface crystallinity of each material was analyzed to identify Fe-bearing minerals using an X-ray diffractometer (XRD; Rigaku Homelab) equipped with a step-ping motor, a graphite crystal monochromator, and a CuK α radiation source (Lu et al., 2016a, b). The total surface area, average pore size, and total pore volume were measured using N₂ sorption on a NOVA 1200 analyzer and calculated using the BET method.

2.3. Batch adsorption experiments and kinetic testing

Batch adsorption experiments were conducted in 55 mL polypropylene tubes using 100 mg of adsorbent and 50 mL phosphorus solutions prepared with sodium phosphate (Sigma Aldrich-342483). Initial phosphorus concentrations of 4, 8, 16, 50, 70 and 90 mg-P/L were tested. As determined by preliminary experiments, adsorption equilibrium was achieved after shaking the tubes for 24 h in a rotary shaker (150 rpm) at room temperature (25 \pm 2 °C) in the dark. The solutions were then centrifuged at 4000 rpm for 15 min. The supernatant was sampled using sterile syringes and passed through 0.22 μ m filters. All adsorption experiments were run in duplicate. Blank solutions, without adsorbent, were used as controls. Phosphorus concentrations of the absorption solution supernatant were obtained using Hach TNT 844 or High range Molybdovanadate testing kits per the Hach method. Phosphorus loaded chars were collected from centrifuge tubes and allowed to dry for 24 h at room temperature in the dark. The P-loaded chars were then analyzed using FTIR and EDS.

2.4. Phosphorus adsorption isotherm

The amount of adsorbed phosphorus per unit biochar mass was calculated using Equation (1) (below).

$$q_e = V(C_0 - C_e)/m, \quad (1)$$

where q_e is the equilibrium adsorbent capacity, C_0 is the initial and C_e is the equilibrium concentration of the phosphorous (mg/L); V is the volume of the solution (L); m is the weight of the adsorbent (g).

To better understand the underlying reaction mechanisms, data was fit to three adsorption isotherm models (below).

$$q_e = \frac{Q_o K_L C_e}{1 + K_L C_e}, \text{ Langmuir} \quad (2)$$

$$q_e = K_f C_e^{\frac{1}{n}}, \text{ Freundlich} \quad (3)$$

$$q_e = (RT \ln A_T / b_T) + (RT \ln C_e / b_T), \text{ Temkin} \quad (4)$$

where: q_e = amount of phosphorus adsorbed per gram of the adsorbent at equilibrium (mg/g); C_e = the equilibrium concentration of adsorbate (mg/L); Q_o = maximum monolayer coverage capacity (mg/g); K_L = Langmuir isotherm constant (L/mg); K_f = Freundlich isotherm constant (mg/g); n = adsorption intensity; A_T = Temkin isotherm equilibrium binding (L/g) constant; b_T = Temkin isotherm constant; R = universal gas constant (8.314 J/mol/K); T = Temperature (K).

To examine the fit of these models, commonly used adsorption error analysis parameters: sum square of errors (ERRSQ) and average relative error (ARE) were calculated using Eq. (5) and Eq. (6) (Ayawei et al., 2017). ERRSQ is said to be one of the most widely used error functions, however, it has a major disadvantage that at higher end liquid-phase adsorbate concentrations it will illustrate a

better fit for experimental data (Ng et al., 2002). To mitigate bias, the ARE function which aims at minimizing the fractional error distribution across the entire concentration range was used in conjunction with ERRSQ (Marquardt et al., 1963).

$$ERRSQ = \sum_{i=1}^n (q_{e,i,calc} - q_{e,i,meas})^2, \text{ Sum square of errors} \quad (5)$$

$$ARE = \frac{100}{n} \sum_{i=1}^n \frac{q_{e,i,calc} - q_{e,i,meas}}{q_{e,i,meas}}, \text{ Average relative error} \quad (6)$$

where $q_{e,i,meas}$ is the experimentally measured adsorbed solid phase concentration of the adsorbate on the adsorbent as determined using Eq. (1) and $q_{e,i,calc}$ is the theoretical concentration of adsorbate on the adsorbent, which has been calculated using one of the isotherm models (i.e. Eq. (2), Eq. (3), or Eq. (4)). (Gupta et al., 2013).

3. Results and discussion

3.1. Fungal growth and nutrient uptake

N. crassa was successfully cultivated on both of the wastewater blends tested. Mature cultures were observed after 48 h of incubation, indicated by the appearance of conidia (fungal spores) across the surface of the fungal mats (Fig. 2a). *N. crassa* depleted large amounts of metal from the growth solutions likely via bio-sorption and metabolic uptake pathways as reviewed by others (Haas, 2003; Rashmi et al., 2004). Larger biomass yields were attained by fungi grown on the PE-BW 1:4 media due to greater accumulation of metal (Fig. 3). ICP-MS analysis of the growth media showed fungi grown under the PE-BW 1:4 media consumed 601.34 mg/L iron, while fungi under the PE-BW 3:4 media consumed only 228.4 mg/L (Fig. 3). In contrast, carbon uptake was favored by fungi grown on the 3:4 dilution (PE-BW 3:4) that consumed about 0.83 g COD/L more than those under the 1:4 ratio (PE-BW 1:4), likely due to the increased availability of supporting nutrients (i.e. nitrogen, phosphorus, etc.). Other constituents that were readily removed from solution during fungal growth included Si, Mg, P and Ca (Fig. 3). These nutrients were likely used to augment the utilization of iron or were bio-mineralized in separate metabolic processes as examined by others (Li et al., 2014). The average dry weight of biomass per liter of media used were 1.77 g for PE-BW 1:4 media and 1.04 g for PE-BW 3:4 media, respectively (Fig. 3).

3.2. Material characterization

Fungal biomass resulting from the PE-BW 1:4 and PE-BW 3:4 growth media were ultimately processed into fungal chars PE-BW 1:4 and PE-BW 3:4. Both finished chars exhibited magnetic properties. PE-BW 1:4 demonstrated a very strong affinity for magnets while PE-BW 3:4 displayed limited attraction (Fig. 2b). After 14 days of being agitated and submerged in aqueous solution (pure water; 0.1 g/L), both chars retained their magnetic properties and were easily recovered from solution using a simple magnet. SEM images of the biochars revealed morphologies unique to each of the materials (Fig. 2c and d). The greater initial metal content of the blend used to generate PE-BW 1:4 led to increased crystalline formation during the pyrolysis process compared to PE-BW 3:4. EDS coupled to the SEM revealed distinct elemental composition of each material surface.

Only a very small amount of elemental carbon (2.1%) was detected in PE-BW 1:4 while PE-BW 3:4 was composed of 23.7%

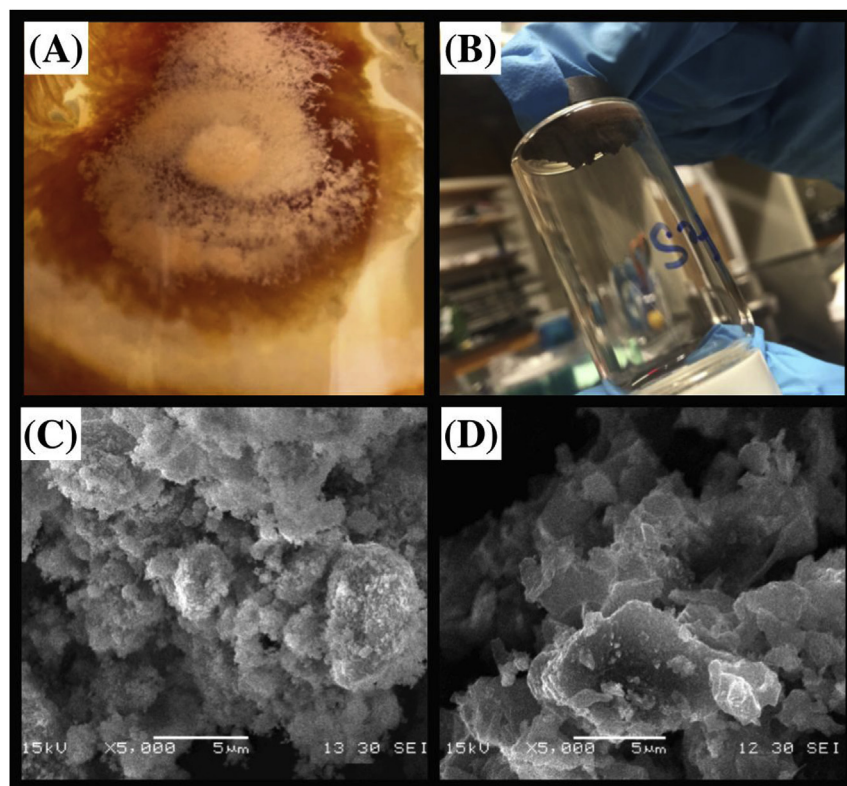


Fig. 2. (A) Fungal cultures grown for 48 h at 37 °C; (B) Magnetic abilities of PE-BW 1:4; SEM image of (C) PE-BW 1:4 and (D) PE-BW 3:4 showing the structure of the materials.

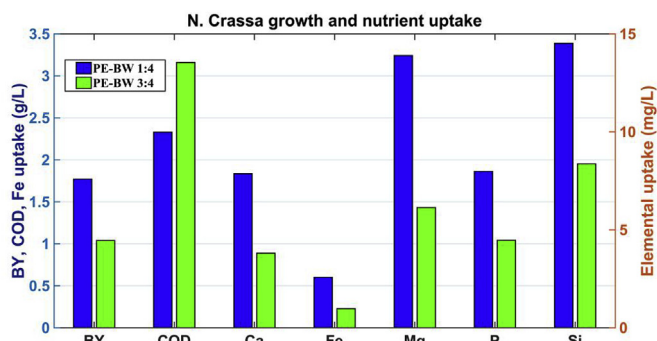


Fig. 3. *N. crassa* growth and nutrient uptake-Biomass yield (BY), COD removal and iron uptake per liter of wastewater used (left y-axis); Ca, Mg, P, Si uptake per liter of wastewater media used (right y-axis).

(Table 1). Both materials retained similar amounts of iron (ca. 45–50%). However, PE-BW 1:4 had a much greater Fe/C ratio (21.4 vs. 2.1) and higher oxygen content (19% vs. 25%) than PE-BW 3:4, which suggested superior iron oxide formation on the material surface. This is line with PE-BW 1:4's enhanced magnetic properties compared to PE-BW 3:4 and the crystal arrangements observed in SEM images. The smaller surface area (51.6 m²/g) and greater average pore diameter (13.2 nm) of PE-BW 1:4 further proposed

amplified iron oxide development as these formations have small surface areas and ample transitional pores (2–50 nm). PE-BW 1:4 had about double the total pore volume (0.2 cm³/g) of PE-BW 3:4 (0.1 cm³/g) even though the carbon content of PE-BW 3:4 was much greater. This may also be attributed to the superior iron oxide formation of PE-BW 1:4 but could also be due to large silica oxide developments in PE-BW 3:4 as implied by its much greater surface silica content.

To further investigate the crystalline structures, FTIR spectra, XPS and XRD patterns were obtained for each of the powdered chars and are provided in the supplemental material section (Fig. S2). XRD analyses identified maghemite (γ -Fe₂O₃) as the major crystalline in PE-BW 1:4 as characterized by strong diffraction peaks at 30.2°, 35.5°, 43.2°, 57.3°, and 62.9° (Machala et al., 2011; Zhang et al., 2013). The presence of maghemite was likely the source of magnetic attraction as proposed in similar work (Tronc et al., 2000). As expected, PE-BW 3:4 showed much weaker maghemite diffraction peaks and presented patterns more similar to an amorphous carbon material. Similar observations were made from the XPS Fe 2p_{3/2} spectra that showed two peaks at 710.6 and 724.1 eV, corresponding to Fe 2p_{3/2} and Fe 2p_{1/2}, that are the characteristic peaks of the Fe³⁺ ion in maghemite. Furthermore, satellite peaks at 719 eV also indicate maghemite formation. In agreement with XRD data, each of the maghemite XPS peaks for PE-BW 1:4 were much stronger than PE-BW 3:4 indicating a greater

Table 1

Major elemental constituents of powdered chars (by weight %), BET-N₂ specific surface area (SA), average pore diameter (APD) and total pore volume (TPV) of biochars.

Material	C (%)	O (%)	Si (%)	Fe (%)	Fe/C	SA (m ² /g)	APD (nm)	TPV (cm ³ /g)
PE-BW 1:4	2.1	23.9	29.8	45.0	21.4	51.6	13.2	0.2
PE-BW 3:4	23.7	19.6	1.4	50.5	2.13	53.0	6.1	0.1

development of maghemite.

FTIR spectra recorded from 400 to 4000 cm^{-1} showed both materials exhibited peaks centered at 432, 556, and 634 cm^{-1} that suggest the presence of Fe–O bonds in the form of maghemite (Andrade et al., 2009; Jubb et al., 2010; Namduri et al., 2008). As expected, PE-BW 1:4 displayed much more pronounced bands than PE-BW 3:4 owing to its greater iron oxide formation. PE-BW 1:4 also showed strong peaks around 831 cm^{-1} that indicate C–O–Fe surface bonds while PE-BW 3:4 displayed broader peaks centered at 1060 cm^{-1} that suggested silica oxide formation in the form of silicone (Si–O–Si). Both materials retained some organic structures as signified by the presence of transitional metal carbonyl groups with peaks centered at 1974 cm^{-1} and 2100 cm^{-1} and broad carboxylate peaks centered at 1600 cm^{-1} (Coates et al., 2000; Chen et al., 2011).

3.3. Phosphorus adsorption isotherms

Both biochars exhibited strong affinities for phosphorus across the range of initial concentrations tested. The highest equilibrium adsorption density of 23.9 mg/g was obtained using PE-BW1:4 and an initial phosphate concentration of 90 mg/L (Fig. 4). This high performance demonstrates the practical use of this material in agricultural and environmental applications. For example, municipal wastewaters commonly contain 5–20 mg/L total phosphorus (Lenntech, 2019). In this range, PE-BW 1:4 achieved an adsorption density of 2.42 mg/g using an initial phosphate concentration of 16 mg/L. In comparable studies, Huggins et al. (2016) reported an adsorption capacity for phosphate of 1.0 mg/g under an initial phosphate concentration of 18 mg/L using a granular biochar prepared from lodgepole pine wood. Moreover, Chen et al. (2011) reported an adsorption capacity of 0.44 mg/g under an under an initial phosphate concentration 12 mg/L using a magnetic biochar orange peel and magnetite deposition.

Others have reviewed the affinity for iron particles to complex phosphorus in detail (Daou et al., 2007; Chen et al., 2011). It is likely the greater phosphorus adsorption ability of PE-BW1:4 stems from its superior maghemite development. Moreover, the higher average pore diameter (13.2 nm vs. 6.1 nm) of PE-BW 1:4 may have further augmented surface interactions with the phosphorus in

solution compared to PE-BW 3:4.

To better understand the underlying sorption behaviors of the phosphorus to the chars, data was fitted to the Freundlich, Temkin, and Langmuir isotherm models. All of the models reproduced the isotherm data fairly well with coefficients of determination (R^2) above 0.90 (Fig. 4). Both PE-BW 1:4 and PE-BW 3:4 fit the Freundlich adsorption isotherm the best. This is best demonstrated by PE-BW 1:4 which exhibited an R^2 value of 0.99 and very low ERRSQ and ARE errors of 33.6 and 35.6, respectively. The Freundlich model is often used to describe chemisorption on heterogeneous surfaces, which is in line with the composite nature of these materials and likely why the data fit this isotherm the best. This was also found by Lů et al. (2013) in similar studies using Fe–Al–Mn trimetal oxides for phosphate removal. Interestingly, the Temkin model which is also commonly used for heterogeneous surfaces was the worst fit for both PE-BW 1:4 and PE-BW 3:4 with R^2 values of 0.91 and 0.94 and large ARE values of 81.2 and 92.9, respectively (Fig. 4). The Temkin model assumes that adsorption is characterized by a uniform distribution of binding energies, which makes it better suited for homogenous materials than the Freundlich model (Dada et al., 2012). In comparison, it may be that the greater homogeneity of PE-BW 3:4, caused by less extensive iron oxide surface formation, made it a better fit to the Temkin model than PE-BW 1:4. This was further suggested by fitting the data to the Langmuir model that assumes that adsorption occurs at specific homogeneous sites on the adsorbent. PE-BW 3:4 fit the Langmuir model almost as well as the Freundlich model with an R^2 of 0.98, ERRSQ of 122.7 and ARE of 27.2 (Fig. 4). PE-BW 3:4 fit the Langmuir model much better than PE-BW 1:4, further indicating that its distinct adsorption mechanisms stem from its greater homogeneity.

3.4. Phosphate retention and surface complexes

To validate the phosphorus recovery capabilities of these materials, EDS and FTIR analyses were conducted on the chars post-adsorption (Fig. S3; Fig. 5). These analyses have been effectively used in many adsorption studies to elucidate interaction mechanisms between adsorbates and adsorbents (Y. Zhang et al., 2005; G. Zhang et al., 2009). At grander scale, EDS confirmed the presence of absorbed phosphorus on the chars. For example, after adsorption

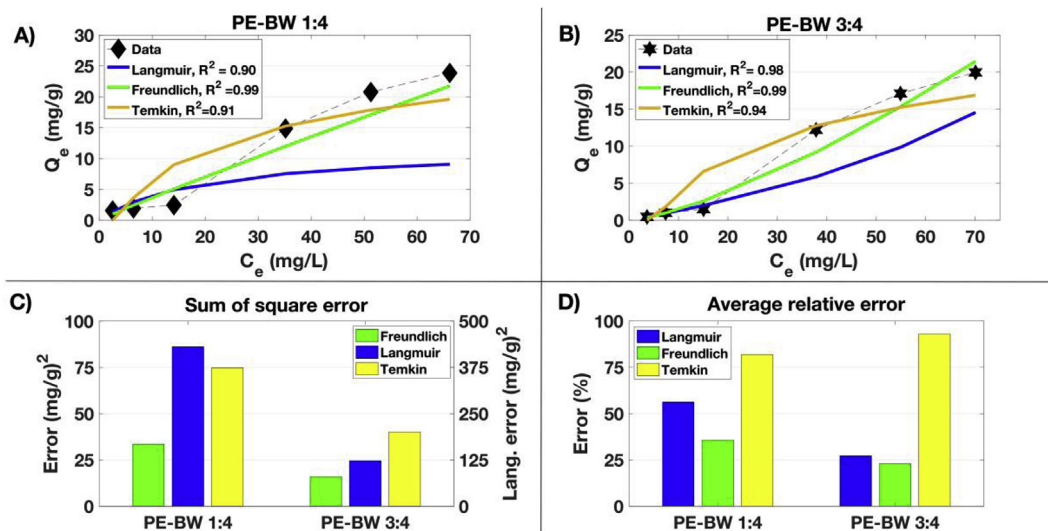


Fig. 4. Adsorption isotherms and error analysis of phosphorus on fungi derived biochars– PE-BW 1:4 adsorption isotherms; \square = measured data (A) PE-BW 3:4 adsorption isotherms; \star = measured data (B) Results of sum of square error analysis; Freundlich and Temkin error (left y-axis), Langmuir (Lang.) error (right y-axis) (C) Results of average relative error analysis for each isotherm fit to measured data (D).

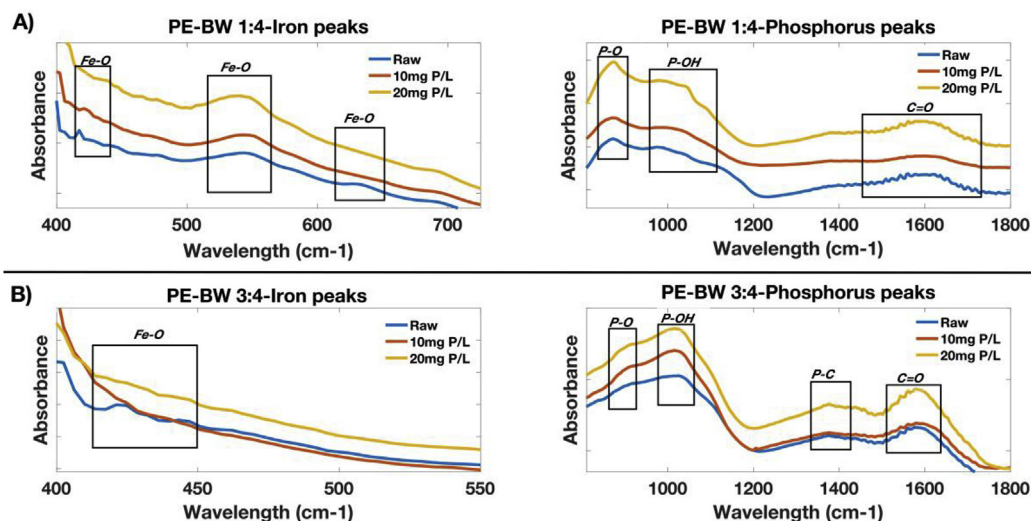


Fig. 5. Phosphorus-loaded biochar FTIR analysis. (A) PE-BW 1:4 iron peaks (left) and phosphorus peaks (right) for raw material and after equilibrium in batch study with 10 mg P/L and 20 mg P/L. (B) PE-BW 3:4 iron peaks (left) and phosphorus peaks (right) for raw material and after equilibrium in batch study with 10 mg P/L and 20 mg P/L.

with an initial phosphate concentration of 50 mg/L, the phosphorus surface atomic percent and weight percent of PE-BW 1:4 rose by 1.52% and 1.76%, respectively. This is complemented by FTIR analyses that showed noteworthy changes even after adsorption with initial concentrations as low as 10 mg/L (Fig. 5).

For both materials, the Fe-O bands centered at 442 cm^{-1} and 634 cm^{-1} seem to lessen and even disappear post adsorption. Conversely, new bands at 865 cm^{-1} and 1025 cm^{-1} appeared after adsorption likely owing to new P-O and P-OH bonds, similar to findings of others (Daou et al., 2007; Lũ et al., 2013). The combined results imply a substitution reaction between Fe-O groups with adsorbed P-ions. Interestingly, PE-BW 3:4 also showed the sharpening of a peak around 1380 cm^{-1} suggesting P-C bonds (Fig. 5). This may demonstrate a second binding mode that is more pronounced in PE-BW 3:4 than PE-BW 1:4, which is expected because PE-BW 1:4 contains much less carbon (2.1% vs. 23.7%). Furthermore, both materials showed elevated peaks around 1600 cm^{-1} which are likely linked to C=O bonding associated with phosphate dissociation on the surface (Coates et al., 2000; Ting Li et al., 2018).

4. Conclusions

A novel bottom-up approach for biofabrication of magnetic biochar has been established. During cultivation, fungi can accumulate large amounts of metals and nutrients from municipal wastewaters allowing for a cheap and sustainable method for generation of biomass feedstock. The resulting fungal biomass can be easily processed into magnetic biochar and the physiochemical properties of the materials can be tuned by controlling fungal growth parameters. The magnetic biochars had viable surface areas ($51.6\text{--}53\text{ m}^2/\text{g}$), average pore sizes ($6.1\text{--}13.2\text{ nm}$), and magnetic capabilities. High phosphorus adsorption capacities of 23.9 mg/g endorsed the use of these materials in environmental applications. Phosphate adsorption on the chars best fit Freundlich isotherms and the results of FTIR and EDS analyses suggested that substitution of surface oxide groups by phosphate were primarily responsible for adsorption. The fungi derived biochars have demonstrated good performance for phosphorus removal and may have numerous applications for adsorption of anionic species such as arsenic from drinking water and chromate for soil remediation. More applications of these magnetic chars are still being explored.

Acknowledgments

The authors also wish to thank peers from across the College of Engineering at the University of Colorado, Boulder for their invaluable insight and helpful suggestions.

Appendix A. Supplementary data

Supplementary data to this article can be found online at <https://doi.org/10.1016/j.jclepro.2019.03.120>.

Funding sources

This work was partially funded by U.S. National Science Foundation under Award CBET-1510682 and the Innovation Center for Geo-Hazards and Eco-Environment in Three Gorges Area.

Declaration of interests

None.

References

- Andrade, A.L., et al., 2009. Synthesis and characterization of magnetic nanoparticles coated with silica through a sol-gel approach. *Cerâmica* 55 (336), 420–424.
- Ayawee, Nimibofa, Newton Ebelegi, Augustus, Wankasi, Donbebe, 2017. Modelling and interpretation of adsorption isotherms. *J. Chem.* 2017.
- Babu, Neelesh, Pathak, Vinay Mohan, 2018. Biosorption of heavy metals: biological approach to control the industrial waste. In: *Handbook of Research on Microbial Tools for Environmental Waste Management*. IGI Global, pp. 270–281.
- Borkovich, Katherine A., et al., 2004. Lessons from the genome sequence of *Neurospora crassa*: tracing the path from genomic blueprint to multicellular organism. *Microbiol. Mol. Biol. Rev.* 68 (1), 1–108.
- Cai, Ru, et al., 2017. Phosphate reclaim from simulated and real eutrophic water by magnetic biochar derived from water hyacinth. *J. Environ. Manag.* 187, 212–219.
- Chen, Baoliang, Chen, Zaiming, Lv, Shaofang, 2011. A novel magnetic biochar efficiently sorbs organic pollutants and phosphate. *Bioresour. Technol.* 102 (2), 716–723.
- Castro-Longoria, E., Vilchis-Nestor, Alfredo R., Avalos-Borja, M., 2011. Biosynthesis of silver, gold and bimetallic nanoparticles using the filamentous fungus *Neurospora crassa*. *Colloids Surfaces B Biointerfaces* 83 (1), 42–48.
- Coates, John, 2000. Interpretation of infrared spectra, a practical approach. In: *Encyclopedia of Analytical Chemistry*.
- Cockrell, A.L., Pirlo, R.K., Babson, D.M., Cusick, K.D., Soto, C.M., Petersen, E.R., Davis, M.J., Hong, C.I., Lee, K., Fitzgerald, L.A., Biffinger, J.C., 2015. Suppressing the *Neurospora crassa* circadian clock while maintaining light responsiveness in continuous stirred tank reactors. *Sci. Rep.* 5, 10691.

- Dada, A.O., et al., 2012. Langmuir, Freundlich, Temkin and Dubinin–Radushkevich isotherms studies of equilibrium sorption of Zn^{2+} onto phosphoric acid modified rice husk. *IOSR J. Appl. Chem.* 3 (1), 38–45.
- Daou, T.J., et al., 2007. Phosphate adsorption properties of magnetite-based nanoparticles. *Chem. Mater.* 19 (18), 4494–4505.
- Gupta, V.K., Tuohy, M.G., 2013. *Biofuel Technologies: Recent Developments*. Springer Science & Business Media.
- Haas, H., 2003. Molecular genetics of fungal siderophore biosynthesis and uptake: the role of siderophores in iron uptake and storage. *Appl. Microbiol. Biotechnol.* 62 (4), 316–330.
- Huggins, Tyler M., et al., 2015. Graphitic Biochar as a cathode electrocatalyst support for microbial fuel cells. *Bioresour. Technol.* 95, 147–153.
- Huggins, Tyler M., et al., 2016. Granular biochar compared with activated carbon for wastewater treatment and resource recovery. *Water Res.* 94, 225–232.
- Jiang, Dan, Amano, Yoshimasa, Machida, Motoi, 2017. Removal and recovery of phosphate from water by calcium-silicate composites–novel adsorbents made from waste glass and shells. *Environ. Sci. Pollut. Control Ser.* 24 (9), 8210–8218.
- Jubb, Aaron M., Allen, Heather C., 2010. Vibrational spectroscopic characterization of hematite, maghemite, and magnetite thin films produced by vapor deposition. *ACS Appl. Mater. Interfaces* 2 (10), 2804–2812.
- Jung, Kyung-Won, Lee, Soonjae, Young, Jae Lee, 2017. Synthesis of novel magnesium ferrite ($MgFe_2O_4$)/biochar magnetic composites and its adsorption behavior for phosphate in aqueous solutions. *Bioresour. Technol.* 245, 751–759.
- Lenntech, 2019. *Water Treatment Solutions*. Lenntech Water Treatment & Purification. www.lenntech.com/phosphorous-removal.htm.
- Li, Qianwei, Laszlo, Csetenyi, Gadd, Geoffrey Michael, 2014. Biomineralization of metal carbonates by *Neurospora crassa*. *Environ. Sci. Technol.* 48 (24), 14409–14416.
- Li, Ronghua, et al., 2016. Recovery of phosphate from aqueous solution by magnesium oxide decorated magnetic biochar and its potential as phosphate-based fertilizer substitute. *Bioresour. Technol.* 215, 209–214.
- Li, Ruining, et al., 2018. Magnetic biochar-based manganese oxide composite for enhanced fluoroquinolone antibiotic removal from water. *Environ. Sci. Pollut. Control Ser.* 25 (31), 31136–31148.
- Li, Ting, et al., 2018. La (OH) 3-modified magnetic pineapple biochar as novel adsorbents for efficient phosphate removal. *Bioresour. Technol.* 263, 207–213.
- Lǔ, Jianbo, et al., 2013. Adsorptive removal of phosphate by a nanostructured Fe–Al–Mn trimetal oxide adsorbent. *Powder Technol.* 233, 146–154.
- Lu, Guolong, et al., 2015. “Synthesis of a conjugated porous Co(II) porphyrinylene–ethynylene framework through alkyne metathesis and its catalytic activity study. *J. Mater. Chem. A* 3, 4954–4959.
- Lu, Lu, et al., 2016a. Nickel based catalysts for highly efficient H_2 evolution from wastewater in microbial electrolysis cells. *Electrochim. Acta* 206, 381–387.
- Lu, Guolong, 2016b. Iron-rich nanoparticle encapsulated, nitrogen doped porous carbon materials as efficient cathode electrocatalyst for microbial fuel cells. *J. Power Sources* 315, 302–307.
- Machala, Libor, Jirí, Tucek, Radek, Zboril, 2011. Polymorphous transformations of nanometric iron (III) oxide: a review. *Chem. Mater.* 23 (14), 3255–3272.
- Marquardt, Donald W., 1963. An algorithm for least-squares estimation of nonlinear parameters. *J. Soc. Ind. Appl. Math.* 11 (2), 431–441.
- Michálek, Richveisová, Barbora, et al., 2017. Iron-impregnated biochars as effective phosphate sorption materials. *Environ. Sci. Pollut. Control Ser.* 24 (1), 463–475.
- Mukherjee, AP, et al., 2008. Green synthesis of highly stabilized nanocrystalline silver particles by a non-pathogenic and agriculturally important fungus *T. asperellum*. *Nanotechnology* 19 (7), 075103.
- Namduri, H., Nasrazadani, S., 2008. Quantitative analysis of iron oxides using Fourier transform infrared spectrophotometry. *Corros. Sci.* 50 (9), 2493–2497.
- Ng, J.C.Y., Cheung, W.H., McKay, G., 2002. Equilibrium studies of the sorption of Cu (II) ions onto chitosan. *J. Colloid Interface Sci.* 255 (1), 64–74.
- Pan, Min, et al., 2017. Kinetic, equilibrium and thermodynamic studies for phosphate adsorption on aluminum hydroxide modified palygorskite nano-composites. *RSC Adv.* 7 (8), 4492–4500.
- Rashmi, K., et al., 2004. Bioremediation of ^{60}Co from simulated spent decontamination solutions. *Sci. Total Environ.* 328 (1–3), 1–14.
- Reza, M. Toufiq, et al., 2015. Production, characterization, and biogas application of magnetic hydrochar from cellulose. *Bioresour. Technol.* 186, 34–43.
- Tronc, E., et al., 2000. Surface-related properties of $\gamma-Fe_2O_3$ nanoparticles. *J. Magn. Magn. Mater.* 221 (1), 63–79.
- Vogel, Henry J., 1964. Distribution of lysine pathways among fungi: evolutionary implications. *Am. Nat.* 98 (903), 435–446.
- Wang, Shengsen, et al., 2015. Removal of arsenic by magnetic biochar prepared from pinewood and natural hematite. *Bioresour. Technol.* 175, 391–395.
- Yang, Qi, et al., 2018. Effectiveness and mechanisms of phosphate adsorption on iron-modified biochars derived from waste activated sludge. *Bioresour. Technol.* 247, 537–544.
- Zhang, Gaosheng, et al., 2009. Removal of phosphate from water by a Fe–Mn binary oxide adsorbent. *J. Colloid Interface Sci.* 335 (2), 168–174.
- Zhang, Ming, et al., 2013. Preparation and characterization of a novel magnetic biochar for arsenic removal. *Bioresour. Technol.* 130, 457–462.
- Zhang, Yu, et al., 2005. Arsenate adsorption on an Fe–Ce bimetal oxide adsorbent: role of surface properties. *Environ. Sci. Technol.* 39 (18), 7246–7253.